Research Square

Preprints are preliminary reports that have not undergone peer review.
They should not be considered conclusive, used to inform clinical practice,
or referenced by the media as validated information.

Continuous absolute-time PIV of 1940-nm thulium fiber laser irrigation: recurrent bidirectional motion and diameter–position associations

Yuhao Bai
Xuanwu Hospital Capital Medical University
Lu Tang
Xuanwu Hospital Capital Medical University
Ying Zhao
zhaoying_a@xwh.ccmu.edu.cn

Xuanwu Hospital Capital Medical University

Research Article

Keywords: Thulium fiber laser, laser-activated irrigation, particle image velocimetry, root canal irrigation, cavitation, endodontics

Posted Date: November 2nd, 2026

DOI: https://doi.org/10.21203/rs.3.rs-10921503/v1

License: This work is licensed under a Creative Commons Attribution 4.0 International License.
Read Full License

Additional Declarations: No competing interests reported.

Title: Continuous absolute-time PIV of 1940-nm thulium fiber laser irrigation: recurrent bidirectional motion and diameter–position associations

Abstract

Purpose: To characterize recurrent root-canal motion across repeated thulium fiber laser (TFL) pulses and test associations of fiber diameter and orifice-relative tip position with sustained axial velocity activity.

Methods: A transparent chamber–canal model evaluated four fiber diameters (150, 200, 275, and 365 μm) at 1 mm above, at, or 1 mm below the canal orifice. Six independent 0.5-s acquisitions were analyzed per condition (72 total). Each acquisition contained 40 pulses (30 mJ, 80 Hz) and 5,000 frames at 10,000 frames/s without phase locking. The primary endpoint was noise-adjusted velocity–time magnitude over the 1.0–9.5-mm canal depth. A robust Gamma-log model tested diameter, position, and their interaction.

Results: All 72 acquisitions contained both apical and coronal 1-ms states above their run-specific signed-noise deadbands. The diameter–position interaction was significant (Wald $\chi^2(6)=403.821$, $p<0.001$). The highest activity occurred with the 365-μm fiber 1 mm below the orifice (26.224 mm; 95% CI 23.977–28.682). Position associations were supported for 200 μm (Holm-adjusted $p=0.009$), 275 μm, and 365 μm (both $p<0.001$), but not 150 μm ($p=0.490$). The overall time-block test had $p=0.1434$, and no late-versus-early contrast survived Holm adjustment.

Conclusion: Continuous absolute-time PIV documented acquisition-scale recurrence of both directions at the study-specific deadband and a diameter–position association. These hydrodynamic findings do not establish exchange, cleaning, pressure, safety, or clinical superiority.

Keywords

Thulium fiber laser; laser-activated irrigation; particle image velocimetry; root canal irrigation; cavitation; endodontics

Introduction

Instrumentation cannot contact every surface of the root-canal system, so irrigants are required to support chemical debridement, dissolution, and microbial control [1, 2]. Irrigation performance and safety depend on solution chemistry, delivery, replenishment, activation, and anatomy [3]. Transparent standardized models permit controlled optical measurements, but their material, geometric, and biological simplifications preclude direct clinical validation [4].

Passive ultrasonic irrigation is driven predominantly by acoustic streaming along a freely oscillating instrument, with an uncertain cavitation contribution [5]. In laser-activated irrigation (LAI), absorbed pulse energy produces vapor-bubble expansion and collapse, liquid displacement, streaming, and pressure transients [6–11]. High-speed imaging also documents repeated displacement and transport of model biofilm fragments [12]. Mechanism and efficacy depend on regimen, geometry, model, and outcome [13], while dissolved solutes can alter bubble behavior [14]. Hydrodynamic activity is therefore not a surrogate for disinfection or cleaning.

Particle image velocimetry (PIV) has quantified the magnitude and spatial propagation

of activated irrigant motion in simulated canals, including movement beyond an anatomic obstruction [15, 16]. In a simulated lateral canal, micro-PIV described alternating inflow and outflow as a bidirectional “breath mode” [17]. More recently, phase-locked micro-PIV resolved pulse-aligned peaks, reversals, transient duration, and wall shear during individual LAI cycles [18]. Such phase-resolved measurements are important for identifying transient mechanisms and peak loading. A continuous absolute-time record asks a different question: whether signed motion recurs across many pulses, how its directional organization varies among acquisitions, and whether activity persists across the activation window. These approaches are complementary rather than competing.

Debris-removal experiments show that the simulated debris removal rate varies with pulse regimen and tip design [19] and that laser-activated irrigation effectively removes artificially placed dentin debris plugs [20]. Transparent-model, PIV, and computational studies show that geometry, delivery rate, tip design, and insertion depth alter velocity, replacement, wall shear, and pressure [21–24]. Ultrasonic and rotary-file PIV likewise show that instantaneous and time-averaged descriptions can differ and that activation setting and depth matter [25–28]. These analogues motivate parameter-sensitive measurement without establishing a universal threshold or TFL-specific mechanism.

A 1940-nm TFL has prior endodontic antibacterial and thermal-dose evidence [29], and water absorbs strongly near this wavelength [30]. Its repeated-pulse irrigation hydrodynamics remain insufficiently characterized. Pressure must also remain a separate safety endpoint: direct Er:YAG measurements show that model anatomy, apical diameter, fiber-tip geometry, and activation conditions influence pressure [31, 32]; pressure therefore remains a separate endpoint that cannot be reconstructed from PIV velocity alone. We therefore used continuous high-speed PIV to test a 4×3 matrix of fiber diameter and orifice-relative tip position. We hypothesized a diameter–position interaction in sustained axial velocity activity and secondarily examined recurrent direction reversal and early-to-late behavior across each 0.5-s, 40-pulse activation.

Materials and methods

Study design and transparent model

The in vitro factorial design comprised fiber diameters of 150, 200, 275, and 365 μm and three tip positions: 1 mm above the canal-orifice plane (P1), at the orifice (P2), and 1 mm below the orifice (P3). Six independent 0.5-s acquisitions were obtained for every cell, giving 72 acquisitions.

The transparent model contained a square simulated pulp chamber with a 6.0-mm internal width above a straight root canal 0.5 mm wide and 12.0 mm long, with the apical end sealed during fabrication (closed-end canal). The model was custom-fabricated in PDMS (Suzhou Wenhao Microfluidic Technology Co., Ltd., Suzhou, China). The irrigant was seeded with 7-μm fluorescent tracer particles (MV-F02; MicroVec Ltd., Beijing, China). The 12-condition design, calibration strategy, measurement domains, and acquisition timeline are summarized in Fig. 1.

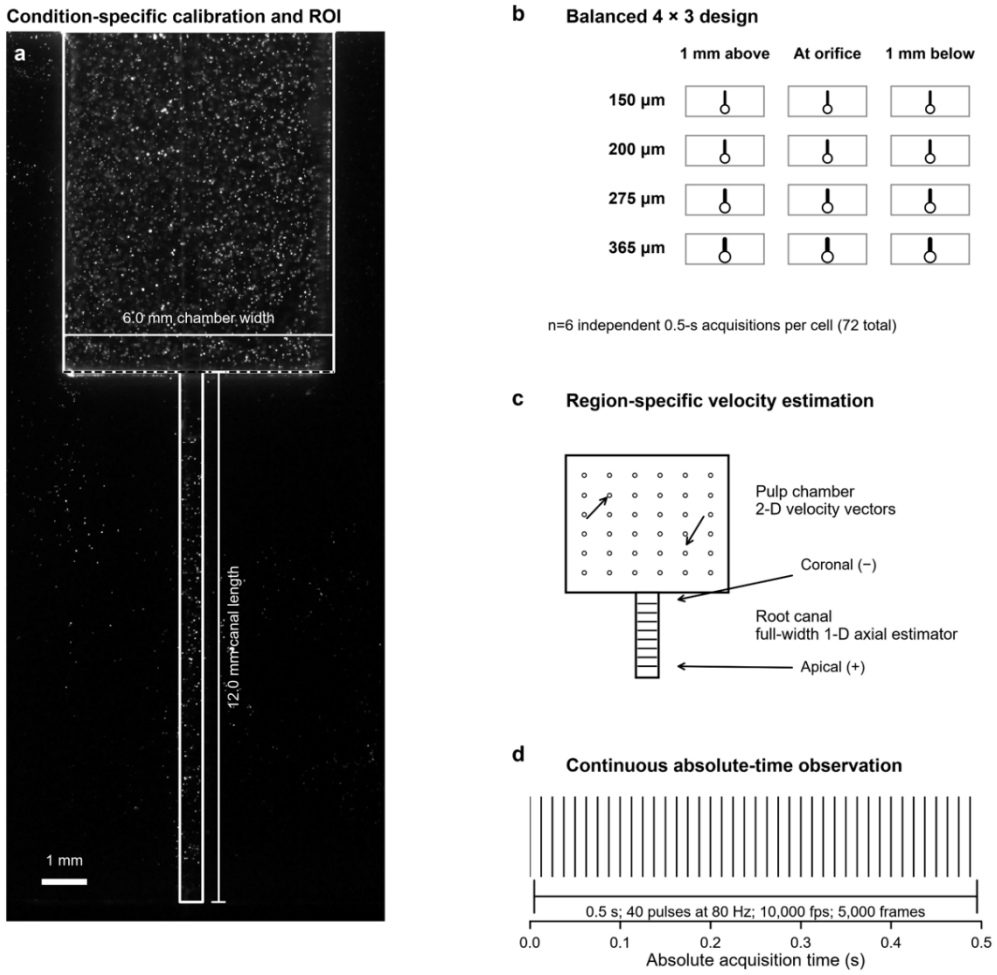


Fig. 1 Experimental design, calibration, measurement domains, and absolute-time acquisition (a) Representative high-speed frame and condition-specific region of interest. (b) Balanced 4 × 3 factorial design with six independent 0.5-s acquisitions per cell. (c) Two-dimensional chamber PIV and full-width one-dimensional root-canal axial estimation. (d) Each acquisition contained 5,000 frames and 40 pulses over 0.5 s; no external phase locking was used

Laser activation and high-speed acquisition

An air-cooled TFL prototype (1940 ± 5 nm; Menovex Medical Technology (Shenzhen) Co., Ltd., Shenzhen, China) was coupled to flat-cleaved bare silica fibers of 150, 200, 275, or 365 µm outer diameter. One setting was used throughout: 30 mJ per pulse, 200 µs pulse duration, and 80 Hz repetition rate, i.e., 2.4 W time-averaged power; dividing pulse energy by pulse width gives an intrapulse power of 150 W under a rectangular-pulse approximation. Pulse energy at the distal fiber tip was measured with a pyroelectric energy meter (Vega console with PE25-C sensor; Ophir Optronics), so the reported 30 mJ is a measured distal-tip value. Before recording, the distal face of every fiber was examined under a Leica S6E stereomicroscope (Leica Microsystems), and any fiber showing cracks, chips, or deformation was rejected. Each acquisition contained 40 pulses over 0.5 s (cumulative energy, 1.2 J) and 5,000 high-speed frames at 10,000 frames/s, producing 4,999 adjacent-frame pairs separated by 100 µs. Camera

acquisition and laser activation were synchronized, but no external phase locking to an individual bubble cycle was used. Images were recorded with a high-speed PIV system built around a FASTCAM NOVA S20 camera (Photron, Japan) fitted with a 100 mm macro lens at 2× magnification. A 30 W 532-nm diode-pumped solid-state laser with light-sheet capability (LA-DP30W; MicroVec Ltd.) illuminated the tracers, and a 200 W LED cold-light source (LUMINOR200A; MicroVec) provided background illumination. Laser emission was monitored through a low-ratio tap on a 2-µm fiber arm feeding an InGaAs photodetector (DET10D2; Thorlabs); a Schmitt trigger reshaped the detector output into a TTL signal for an eight-channel programmable synchronizer (MicroPulse825; MicroVec), which delivered TTL trigger signals to all hardware components with 250-ps accuracy, and the timing chain was examined on a DSOX1202G oscilloscope (Keysight Technologies). Irradiance and radiant exposure were not treated as measured explanatory variables because distal energy, emitting area, and beam profile were not independently established (Table 1).

Table 1. Key experimental, acquisition, image-analysis, and statistical parameters.

Domain	**Parameter**	**Value**
Laser	Wavelength/source	1940 ± 5 nm air-cooled thulium fiber laser prototype
Laser	Pulse energy	30 mJ (measured at the distal fiber tip)
Laser	Pulse repetition frequency	80 Hz
Laser	Pulse duration	200 µs
Laser	Intrapulse power	150 W (rectangular-pulse approximation)
Laser	Average power	2.4 W
Laser	Output calibration/stability	Distal-tip pulse energy measured with a pyroelectric energy meter (Vega console, PE25-C sensor; Ophir Optronics); distal faces screened with a Leica S6E stereomicroscope and damaged fibers rejected
Delivery	Fiber diameters	150, 200, 275, and 365 µm outer diameter; flat-cleaved bare silica fibers
Delivery	Fiber-tip positions	1 mm above, at, or 1 mm below the canal-orifice plane
Delivery	Laser/fiber manufacturer details	Laser: Menovex Medical Technology (Shenzhen) Co., Ltd., Shenzhen, China; flat-cleaved bare silica fibers
Activation	Per independent acquisition	0.5 s; 40 pulses; cumulative energy 1.2 J
Model	Internal geometry	6.0-mm chamber width; 0.5-mm canal width; 12.0-mm canal length
Model	Manufacture and terminal geometry	Custom-fabricated in PDMS (Suzhou Wenhao Microfluidic Technology Co., Ltd., Suzhou, China); canal sealed at the apical end during fabrication (closed-end configuration)

Domain	Parameter	Value
Irrigant	Composition and handling	Seeded with 7-µm fluorescent tracer particles (MV-F02; MicroVec Ltd., Beijing, China)
Tracer	Seeding particles	7-µm fluorescent particles (MV-F02; MicroVec Ltd., Beijing, China)
Imaging	Acquisition	10,000 frames s^{-1}; 5,000 frames/acquisition; 100-µs adjacent-frame interval; not phase locked
Imaging	Optical hardware and synchronization	FASTCAM NOVA S20 camera (Photron) with 100 mm macro lens at 2× magnification; LA-DP30W 532-nm DPSS light sheet and LUMINOR200A LED (MicroVec); MicroPulse825 eight-channel synchronizer (MicroVec; 250-ps TTL accuracy); DET10D2 InGaAs photodetector (Thorlabs); DSOX1202G oscilloscope (Keysight)
Calibration	Per-condition calibration/ROI	Repeated for each of 12 conditions and registered to six acquisitions/condition
PIV	Pulp-chamber quantitative pipeline (all 72 acquisitions)	MicroVec Pro v7.5 (MicroVec, Beijing, China); two-dimensional normalized cross-correlation; 32×32-px interrogation window, 96×96-px search region, 16-px step
PIV	Root-canal quantitative pipeline (all 72 acquisitions)	MicroVec Pro v7.5; full-width one-dimensional axial estimator; 32-px axial window, ±26-px search, 8-px step
PIV	Fig. 2 chamber visualization only	MicroVec Pro multipass window-deformation schedule with 96→64→32→24-px interrogation windows and 72→32→16→12-px overlaps (final spacing 12 px); three-field raw-vector median where ≥2/3 supported; no interpolation; excluded from the 72-acquisition endpoint and inference
Primary endpoint	Definition	Noise-adjusted integral of absolute full-width axial velocity over the supported depth-time domain; unit: mm velocity–time magnitude
Statistics	Inferential platform/models	IBM SPSS Statistics 27.0.1.0; primary Gamma-log model and sensitivity/simple-effect/multiplicity-adjusted comparisons; temporal generalized estimating equations with robust covariance

Abbreviations: PIV, particle image velocimetry; ROI, region of interest.

Calibration, measurement domains, and PIV processing

Before PIV calculation, the pixel scale of the high-speed images was converted to physical dimensions, and the data then entered the processing pipeline. Calibration and region-of-interest review were repeated for each condition and registered to its six acquisitions. Between-condition analysis used the common 1.0–9.5-mm depth below

the orifice.

PIV infers velocity from particle-image displacement over a known time interval [33]. Cross-correlation performance depends on particle-image density, displacement, interrogation dimensions, and dynamic range [34]. The quantitative pipeline for all 72 acquisitions was implemented in MicroVec Pro (v7.5, MicroVec, Beijing, China) with Python-based aggregation and applied two-dimensional local normalized cross-correlation in the chamber with a 32×32-pixel interrogation window, a 96×96-pixel search region, and a 16-pixel step. Chamber-vector acceptance required correlation quality ≥4, peak correlation ≥0.10, ≥8 tracer pixels, displacement ≤32 pixels per component, and local-median difference ≤4 pixels. Because the canal was only approximately 25 pixels wide, the same quantitative pipeline used a full-width one-dimensional axial normalized cross-correlation estimator with a 32-pixel axial window, a ±26-pixel search, and an 8-pixel step. Root-vector acceptance required the corresponding thresholds of ≥4, ≥0.10, ≥8 pixels, absolute axial displacement ≤24 pixels, and local-median difference ≤5 pixels. Accordingly, two-dimensional canal vectors, canal streamlines, transverse velocity, volumetric flow, and near-wall shear were not inferred.

The dynamic bright mask used the greater of 1,200 digital numbers and the pair-specific 99.98th intensity percentile. Connected components ≥20 pixels were dilated by 5 pixels; a vector window with >5% bright occupancy was invalid. Invalid vectors remained missing, without interpolation. The local consistency screen followed robust normalized-median outlier detection [35]. Run inclusion required all 4,999 pairs, 40 detected pulses, a median pulse interval within ±2 pairs of the expected 125-pair interval, and root and chamber valid-cell fractions and valid-time coverages each ≥0.60. All 72 acquisitions met these criteria.

Implementation validation used 432 idealized rigid axial shifts from −20 to +20 pixels across particle-density and noise settings. Recovery gave r=1.00000, slope=0.99998, bias=0.0000 pixels, mean absolute error=0.0033 pixels, root mean square error=0.0050 pixels, and sign agreement=1.000. Across 500 additional noise, linear-shear, bright-occlusion, and particle-dropout trials, scenario-median vector mean absolute errors ranged from 0.013 to 0.162 pixels and median sign agreement was 1.000; the bright-occlusion 95th-percentile trial error was 0.788 pixels. These implementation checks did not quantify full image-matching uncertainty [36] or validate refraction, out-of-plane motion, particle fidelity, or a universal threshold. Particle-intensity variation and subpixel limitations further support a study-specific detection floor [37].

For Fig. 2, the quality-controlled F200_P2 acquisition nearest the within-cell median primary endpoint was selected before visualization. Eligible pulse windows 2–39 lasted ≥10 ms, had ≥95% temporal coverage, contained both root directions above the deadband, and supported ≥70% of root depths and ≥90% of chamber cells at both states. The interval nearest the within-run median of the smaller directional component was chosen, with the earlier interval breaking a tie. Chamber-only fields used MicroVec Pro symmetric multipass windows of 96→64→32→24 pixels with overlaps of

72→32→16→12 pixels (final spacing, 12 pixels). Thus, 24 pixels was the final fourth-pass window, not a second-pass analysis or the 32-pixel quantitative pipeline in Table 1. Displays were componentwise medians of three adjacent raw fields, required ≥2/3 native support, and left unsupported cells transparent without interpolation, inpainting, or wall extrapolation. Root panels retained the quantitative one-dimensional profile. None of these displays entered the endpoint or inference.

Outcomes

Within each acquisition, the 20% of adjacent-frame pairs with the lowest acquisition-wide image-activity score were identified; the score was the 99th percentile of absolute intensity difference in each downsampled image pair. At each canal depth, the median absolute axial velocity in this common low-activity set defined a lower envelope; the run-level signed deadband was the median of these depth-specific envelopes. For the primary endpoint, the envelope was subtracted from absolute axial velocity and negative residuals were set to zero. Each time-point mean across 1.0–9.5 mm required at least 20% finite spatial support; otherwise it remained missing. The mean of finite time points was multiplied by 0.4999 s, standardizing every acquisition to the complete interval. This sustained axial velocity activity has units of millimeters of velocity–time magnitude; "sustained" denotes integration over the fixed interval, not uninterrupted motion. It is not particle displacement, net transport, irrigant-exchange volume, mixing efficiency, pressure, or cleaning efficacy, and the lower envelope is not a sham or laser-off control.

For direction-state analysis, the signed full-width axial series was median-filtered over three adjacent pairs and summarized in non-overlapping 1-ms absolute-time bins. A bin required at least 5 of its 10 constituent pairs; otherwise it was missing. It was classified as apical (+), coronal (−), or inside the run-specific deadband. The active fraction was the proportion of all 1-ms bins classified as apical or coronal. To count direction transitions, missing and deadband bins were removed and sign changes between consecutive retained states were counted. Recurrence required both directions and repeated transitions within an acquisition; it was descriptive, used a study-specific detection threshold, and imposed no clinical-effectiveness threshold. Secondary endpoints included apical and coronal velocity–time components and their smaller-to-larger ratio. The 40 pulse windows were grouped a priori as early (pulses 1–13), middle (14–27), and late (28–40).

Statistical analysis

One independent 0.5-s acquisition was the experimental unit (N=72; n=6 per cell); frames, time bins, depth points, and vector cells were nested measurements and did not increase n, consistent with established safeguards against pseudoreplication [38, 39]. The primary SPSS 27 model used a Gamma distribution, log link, robust covariance, and fixed categorical effects for fiber diameter, tip position, and their interaction. Joint simple effects were Holm-adjusted across seven strata, and pairwise comparisons were Bonferroni-adjusted within each stratum, with the adjustment applied jointly to p values and confidence intervals. Sensitivity models used raw activity, an observed-coverage

integral assigning zero to unsupported time points, adjustment for centered within-condition acquisition order, adjustment for valid-cell fraction, and robust normal modeling of the log endpoint.

Duration-normalized early, middle, and late activity was log transformed and analyzed by generalized estimating equations with robust covariance, acquisition-level clustering, an AR(1) working correlation, and fiber×position×time-block terms. Cluster-aware analysis was used because time-block observations were nested within acquisitions [40]. The four temporal omnibus tests were exploratory and unadjusted; 12 late-versus-early condition contrasts were Holm-adjusted. Exchangeable and independent working correlations were sensitivity analyses. Two-sided α was 0.05.

Software roles and reproducibility

PIV analysis used MicroVec Pro (v7.5, MicroVec, Beijing, China) with Python-based post-processing for all 72 acquisitions, covering image-pair processing, masking, vector quality control, and acquisition-level and time-block endpoints. The same software route generated the Fig. 2 chamber visualization fields. IBM SPSS Statistics 27.0.1.0 generated every reported inferential estimate, confidence interval, test, and adjusted p value, including the Gamma-log and sensitivity models, simple and pairwise comparisons, and temporal generalized estimating equations. SPSS syntax, data, output, and exported tables were archived. Python statistical code served only as an independent reconciliation: 239/239 same-estimand comparisons agreed with SPSS within an absolute or relative tolerance of 1×10^{-6}, and no Python inferential value replaced a reported SPSS result. Matplotlib [41] rendered the prespecified endpoints and SPSS exports without refitting; PowerPoint and Origin provided editable assembly only. PIVlab 3.14 [42] only cross-checked fixed image pairs from the Fig. 2 chamber route and generated no study endpoint or inference.

Results

Data completeness and representative flow fields

All 72 acquisitions passed the run-level quality criteria and contributed 359,928 adjacent-frame pairs. Mean condition-level valid-vector fractions ranged from 0.859 to 0.999 in the canal and from 0.990 to 1.000 in the chamber. In F365_P3, the mean root valid-vector fraction was 0.9858 and the mean root bubble-mask fraction was 0.0053; its high endpoint was therefore not a direct consequence of widespread bubble masking. Masked bright regions remained missing rather than being imputed. Restriction to the common depth prevented a cropped field boundary from being interpreted as the apex.

Fig. 2 places one event, deterministically selected using the prespecified rule, within its full 0.5-s record. In F200_P2_R02, the interval changed from −10.845 mm/s coronal at 184.35 ms to +22.599 mm/s apical at 188.65 ms, 4.3 ms later. The visualization-only chamber fields show local two-dimensional direction, whereas the root panels retain the quantitative full-width axial depth profiles. The event is descriptive, not a phase-resolved bubble-cycle reconstruction.

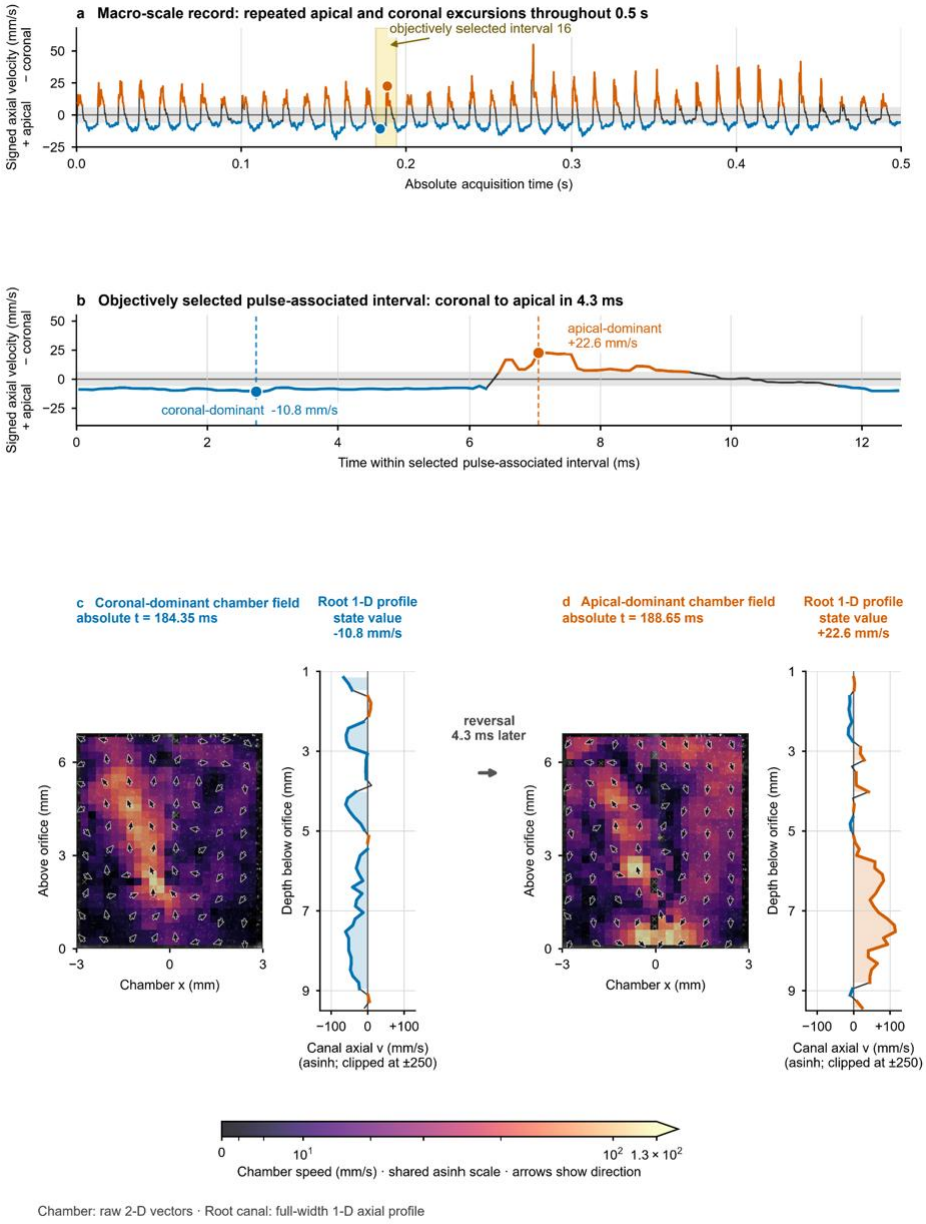


Fig. 2 Bridge from the 0.5-s root endpoint to a deterministically selected bidirectional interval in F200_P2_R02 **The coronal and apical states occurred at 184.35 and 188.65 ms, 4.3 ms apart. Chamber overlays are componentwise medians of three adjacent raw fields from the separate visualization route with a 24-pixel final pass and are displayed only where at least two native fields were valid; unsupported cells remain transparent. Root panels retain the quantitative full-width one-dimensional axial profile. Arrow orientation indicates direction rather than speed magnitude. The event and chamber visualization did not contribute to the 72-acquisition endpoint or inference**

Recurrent bidirectional root-canal motion

Every acquisition (72/72) contained both apical and coronal 1-ms states above its run-specific signed-noise deadband (Fig. 3). After deadband and missing bins were removed, direction-transition counts per acquisition had a minimum, median, and maximum of 15, 77, and 80. The corresponding active fractions were 0.144, 0.674, and

0.858, and every acquisition contained at least 46 apical and 13 coronal bins. Across 0.5×, 0.75×, and 1.0× deadbands, 72/72 acquisitions remained bidirectional; at 2.0×, 63/72 (87.5%) did so, with transition count 0/19/79 (minimum/median/maximum). These descriptive distributions support recurrent bidirectional motion at the study's measurement scale, but their threshold dependence and absence of a sham or transport endpoint preclude claims of laser-attributable exchange or cleaning. Bidirectionality was not necessarily symmetric: in F365_P3, the mean apical and coronal velocity–time components were 15.004 and 11.221 mm, respectively (smaller-to-larger ratio, 0.748).

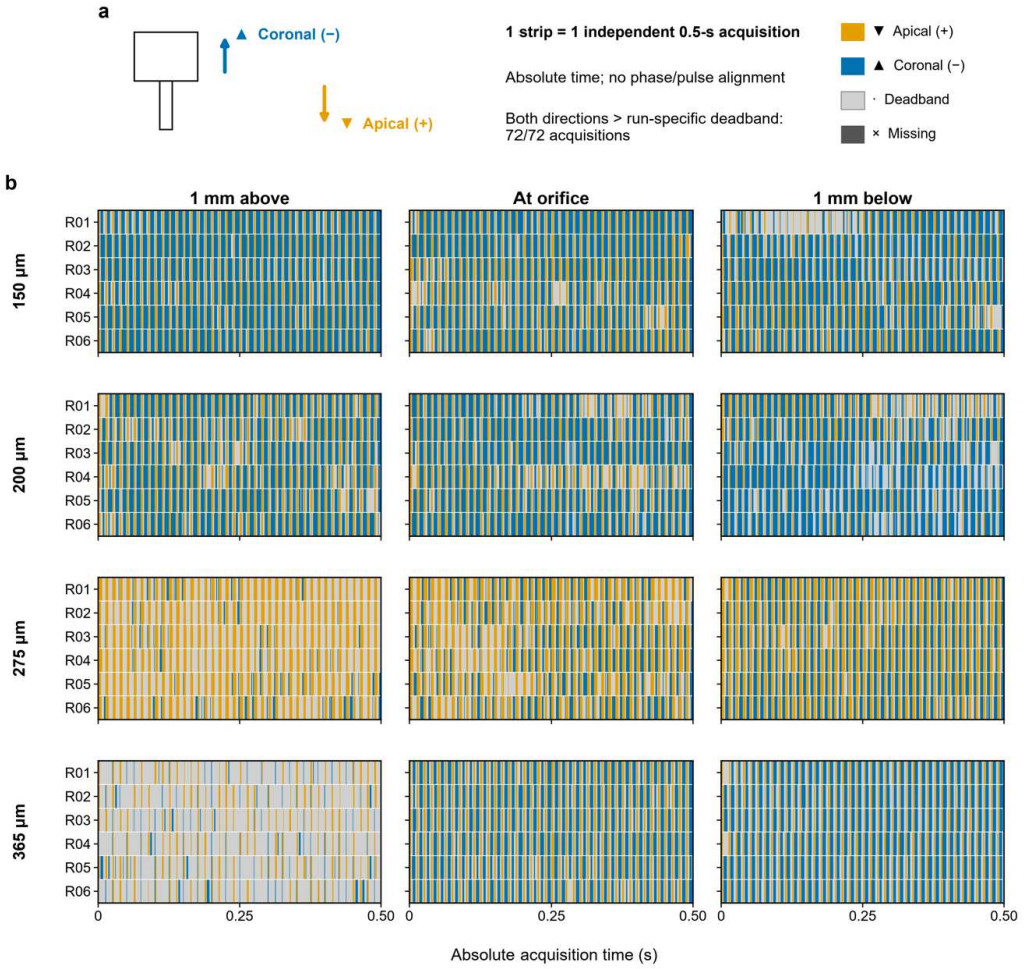


Fig. 3 Macro-scale bidirectional root-canal motion across 72 independent acquisitions (a) Direction convention and redundant color/symbol key. (b) Each row is one 0.5-s acquisition and each column is a non-overlapping 1-ms absolute-time bin. Apical (+) and coronal (−) states exceeded the run-specific signed-noise deadband; gray indicates the deadband and dark gray indicates missing data. All acquisitions contained both directions at the primary threshold, whereas 63/72 did so at twice that threshold. The raster is descriptive, is not pulse normalized, and does not establish laser-attributable transport without a sham

Diameter–position association

The 12 model-estimated cell means and robust 95% confidence intervals are reported in Table 2. Estimates ranged from 2.118 mm (95% CI 1.751–2.562) for F200_P1 to 26.224 mm (95% CI 23.977–28.682) for F365_P3.

Table 2. Model-estimated primary endpoint by fiber diameter and tip position.

Fiber diameter (μm)	1 mm above	At orifice	1 mm below
150	5.548 (5.194–5.926)	6.603 (4.665–9.348)	5.085 (3.955–6.537)
200	2.118 (1.751–2.562)	2.811 (2.455–3.219)	3.101 (2.734–3.516)
275	3.031 (2.709–3.391)	4.296 (4.019–4.593)	6.984 (6.372–7.654)
365	3.767 (3.492–4.064)	15.069 (14.546–15.612)	26.224 (23.977–28.682)

Values are SPSS 27 Gamma-log model estimates (95% confidence intervals) in millimeters of noise-adjusted absolute axial velocity–time magnitude; the endpoint is not net displacement.

The fiber-diameter×tip-position interaction was significant (Wald $\chi^2(6)=403.821$, $p<0.001$; Fig. 4 and Table 3). The interaction remained $p<0.001$ with raw activity, the observed-coverage endpoint, centered-order adjustment, valid-fraction adjustment, and robust log-scale normal modeling. These sensitivities address endpoint and covariate choices; they do not remove the small-cell limitations of robust Wald inference. Fig. 4 therefore retains all observations as the primary descriptive display. Position was not associated with the endpoint for the 150-μm fiber, showed a modest association for 200 μm, and showed progressively stronger gradients for 275 and 365 μm. Fiber-diameter effects were detected at every position, although their ordering varied by position. Exact simple-effect and adjusted pairwise estimates are reported in Table 3.

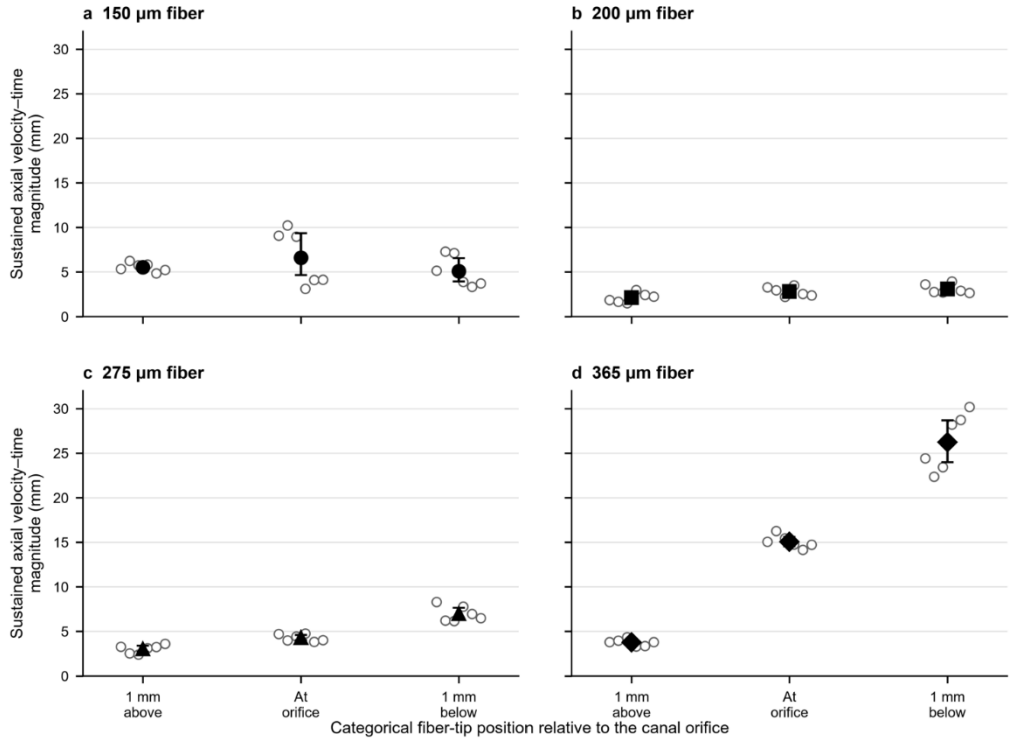


Fig. 4 Fiber-diameter × tip-position interaction for sustained axial velocity–time magnitude Open circles show six independent acquisitions per cell; filled symbols show SPSS 27 Gamma-log estimates with robust 95% confidence intervals. Tip position is categorical and estimates are not connected. The endpoint is velocity–time magnitude, not net irrigant displacement

Table 3. Inferential summary of the primary and exploratory temporal analyses.

Analysis	Effect	Estimate or test	p value	Multiplicity
Primary omnibus	Fiber diameter	Wald χ^2=1290.888; df=3	<0.001	Unadjusted omnibus
Primary omnibus	Tip position	Wald χ^2=256.754; df=2	<0.001	Unadjusted omnibus
Primary omnibus	Fiber diameter × tip position	Wald χ^2=403.821; df=6	<0.001	Unadjusted omnibus
Primary simple effect	Tip position within fiber: 150 µm	Wald χ^2=1.427; df=2	0.490	Holm across 7 joint simple effects
Primary simple effect	Tip position within fiber: 200 µm	Wald χ^2=10.779; df=2	0.009	Holm across 7 joint simple effects
Primary simple effect	Tip position within fiber: 275 µm	Wald χ^2=136.905; df=2	<0.001	Holm across 7 joint simple effects
Primary simple effect	Tip position within fiber: 365 µm	Wald χ^2=1326.017; df=2	<0.001	Holm across 7 joint simple effects
Primary simple effect	Fiber diameter within position: 1 mm above	Wald χ^2=158.551; df=3	<0.001	Holm across 7 joint simple effects
Primary simple effect	Fiber diameter within position: At orifice	Wald χ^2=1458.631; df=3	<0.001	Holm across 7 joint simple effects
Primary simple effect	Fiber diameter within position: 1 mm below	Wald χ^2=864.183; df=3	<0.001	Holm across 7 joint simple effects
Position pairwise	150 µm: At orifice vs 1 mm above	Ratio=1.190 (CI 0.773–1.834)	1.000	Bonferroni within fiber
Position pairwise	150 µm: 1 mm below vs 1 mm above	Ratio=0.917 (CI 0.667–1.259)	1.000	Bonferroni within fiber
Position pairwise	150 µm: 1 mm below vs At orifice	Ratio=0.770 (CI 0.456–1.300)	0.697	Bonferroni within fiber
Position pairwise	200 µm: At orifice vs 1 mm above	Ratio=1.327 (CI 0.998–1.765)	0.052	Bonferroni within fiber
Position pairwise	200 µm: 1 mm below vs 1 mm above	Ratio=1.464 (CI 1.108–1.934)	0.003	Bonferroni within fiber
Position pairwise	200 µm: 1 mm below vs At orifice	Ratio=1.103 (CI 0.880–1.382)	0.894	Bonferroni within fiber
Position pairwise	275 µm: At orifice vs 1 mm above	Ratio=1.417 (CI 1.209–1.662)	<0.001	Bonferroni within fiber

Analysis	Effect	Estimate or test	p value	Multiplicity
Position pairwise	275 μm: 1 mm below vs 1 mm above	Ratio=2.304 (CI 1.931–2.750)	<0.001	Bonferroni within fiber
Position pairwise	275 μm: 1 mm below vs At orifice	Ratio=1.626 (CI 1.415–1.867)	<0.001	Bonferroni within fiber
Position pairwise	365 μm: At orifice vs 1 mm above	Ratio=4.000 (CI 3.611–4.430)	<0.001	Bonferroni within fiber
Position pairwise	365 μm: 1 mm below vs 1 mm above	Ratio=6.961 (CI 6.031–8.034)	<0.001	Bonferroni within fiber
Position pairwise	365 μm: 1 mm below vs At orifice	Ratio=1.740 (CI 1.547–1.958)	<0.001	Bonferroni within fiber
Temporal omnibus	Time block	Wald χ^2=3.885; df=2	0.1434	Exploratory unadjusted omnibus
Temporal omnibus	Fiber diameter × Time block	Wald χ^2=16.830; df=6	0.0099	Exploratory unadjusted omnibus
Temporal omnibus	Tip position × Time block	Wald χ^2=1.492; df=4	0.8281	Exploratory unadjusted omnibus
Temporal omnibus	Fiber diameter × Tip position × Time block	Wald χ^2=10.860; df=12	0.5410	Exploratory unadjusted omnibus
Temporal contrasts	Late vs early within each of 12 conditions	Rate-ratio range 0.703–1.106; 0/12 significant	minimum Holm p=0.082	Holm across 12 contrasts

Wald tests used robust covariance. Multiplicity adjustments are specified in the final column. For each fiber diameter, the three within-fiber position comparisons were generated by SPSS GENLIN with Bonferroni adjustment applied jointly to both p values and confidence intervals. Thus, the displayed intervals have 95% familywise coverage within each three-comparison stratum (98.33% per-comparison confidence level); they are not ordinary pointwise 95% intervals.

Directional components and temporal persistence

Apical and coronal components varied among conditions and among the six acquisitions within a condition (Fig. 5a). The exploratory overall time-block effect was not significant (Wald $\chi^2(2)$=3.885, p=0.1434). The fiber×time-block term had p=0.0099, whereas position×time had p=0.8281 and fiber×position×time had p=0.5410. No condition-specific late-versus-early activity-rate contrast survived Holm adjustment; the adjusted p values had a minimum of 0.082. Exchangeable and independent working-correlation sensitivities did not change the temporal omnibus conclusions.

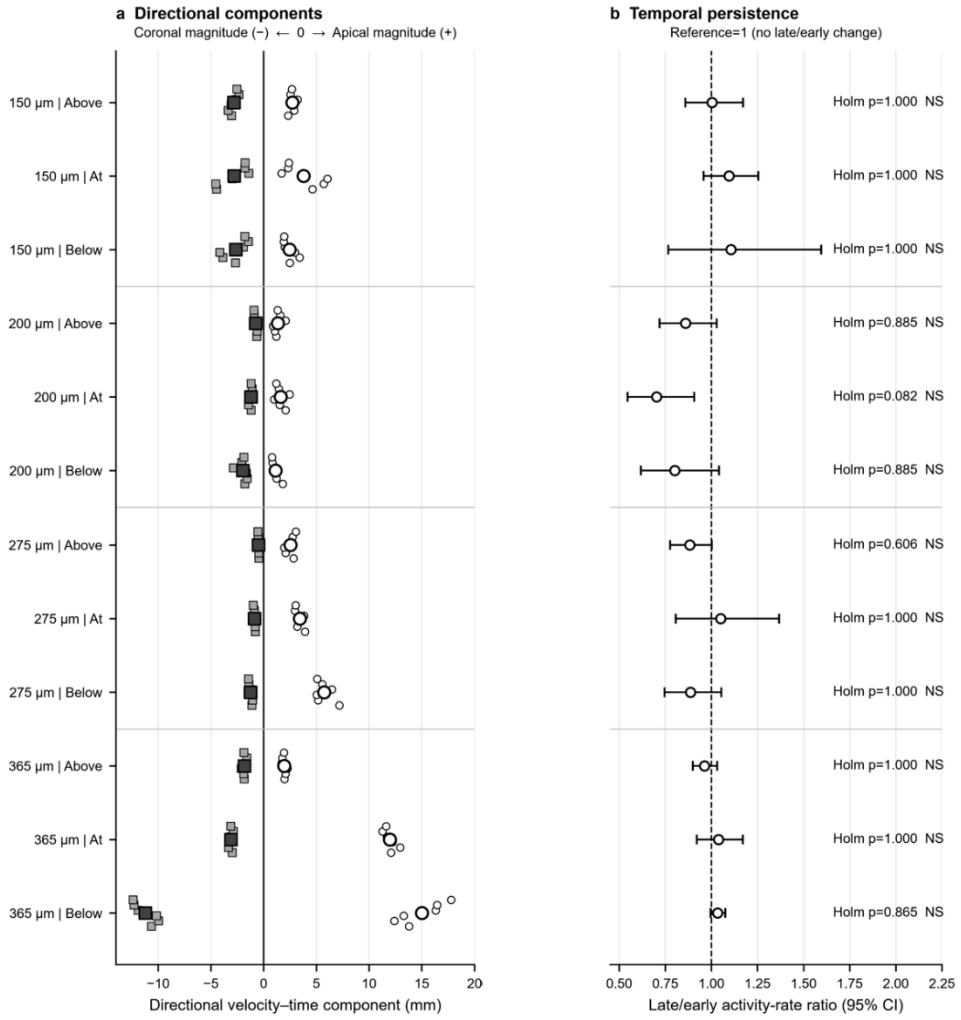


Fig. 5 Directional components and within-acquisition temporal persistence (a) Apical (+) and coronal (−) velocity–time components for six acquisitions per condition; large symbols denote cell means. (b) SPSS 27 GEE late/early activity-rate ratios with pointwise 95% confidence intervals. Holm-adjusted p values are shown for all 12 contrasts; none was significant. Frames and time bins were not independent samples

Discussion

Both directions recurred within every 0.5-s, 40-pulse acquisition, reflecting repeated changes rather than a condition-averaged waveform or selected event. Diameter–position patterns varied, with the steepest gradient for 365 µm/P3. Sensitivity analyses did not resolve the small-cell inference limitation.

The present method complements phase-locked micro-PIV, which aligns cycles to resolve peaks, reversal timing, transient duration, and, when wall resolution permits, wall shear [18]. Without phase registration, this experiment cannot reconstruct one bubble's complete expansion–collapse history. Retaining absolute time instead tested recurrence over 0.5 s and early-to-late behavior. The 72-run raster addresses acquisition-scale recurrence; the selected event only bridges local chamber and canal behavior.

The prior “breath mode” described alternating motion in a simulated lateral canal [17]. The present main-canal pattern is analogous, not the same established phenomenon, and does not prove apical irrigant renewal. Exchange requires concentration, tracer-replacement, or volumetric transport measurement. The nonsignificant overall time-block test and Holm-adjusted late/early contrasts showed no uniform accumulation or decay pattern over 0.5 s; they do not prove constancy, particularly with six acquisitions per cell.

The 365-µm/P3 condition had the largest velocity–time magnitude. With an outer diameter of 365 µm, the fiber occupies 73% of the 500-µm canal width, leaving 135 µm total diametral clearance when centered. Deeper placement could reduce coronal bypass and strengthen axial coupling. Cavity dimensions and tip geometry affect bubble oscillation and pressure in laser-irrigation models [8, 10, 11], but confinement remains untested here because wall proximity, centering, bubble morphology, optical emission, and hydrodynamic confinement were not varied independently. The F365_P3 directional components were not exclusively apical; their 0.748 smaller-to-larger ratio argues against one-way pumping.

Equal measured distal-tip pulse energy and power do not establish equal irradiance across diameters. Under a simple equal-output, uniformly emitting-aperture model, dose per area would decrease as diameter increased; the observed maximum at 365 µm/P3 was not consistent with that model. This does not identify the mechanism because emitting-core size, outside diameter, beam profile, numerical aperture, distal energy, losses, and stability were incompletely measured and confounded with diameter. Direct distal dosimetry and independent manipulation of confinement are needed to separate optical from geometric contributions [9, 29, 30].

For 150 µm, the position joint test was not significant; wider clearance could permit coronal bypass, but this was not measured. Mean chamber speed–time activity was 3.534, 3.546, and 3.217 mm at P1, P2, and P3, so the hypothesized P3 chamber increase was absent. The 200-µm association was modest but not absent, whereas 275 µm showed a stepwise gradient and 2.304-fold P3/P1 estimate. Grouping all non-365-µm fibers as unchanged would therefore be inaccurate. Position dependence strengthened at 275 and 365 µm, rather than demonstrating a mechanism unique to 365 µm.

Bidirectional motion is a hydrodynamic screening property, not an efficacy measure. F365_P3 warrants exchange and cleaning tests but is not established as optimal; greater activity might coexist with pressure, extrusion, temperature, or tissue loading. Pressure findings from other laser systems do not transfer directly to this TFL setup [31, 32]. Follow-up should combine continuous PIV with pressure, extrusion or concentration-exchange, and thermal measurements.

The single straight transparent model improved optical access but did not reproduce dentin, complex anatomy, tissue, debris, or the range of clinical irrigants [4]. Six acquisitions per cell limit small-sample sandwich inference, and no laser-off sham or active comparator was included; the within-run lower envelope was not a sham baseline. The approximately 25-pixel canal supported only full-width one-dimensional axial

estimates, and planar PIV captured neither volumetric exchange nor out-of-plane motion. Exchange, cleaning, antimicrobial effects, pressure, extrusion, temperature, tissue response, and clinical outcomes were not measured. F365_P3 therefore warrants efficacy-and-safety testing but is not established as an optimal or clinically safe setting.

Conclusion

Across 72 independent 0.5-s acquisitions, continuous absolute-time PIV documented recurrent apical and coronal root-canal motion during repeated 1940-nm TFL activation. Fiber diameter and tip position were strongly associated with sustained axial velocity activity, with the largest estimate for 365 µm placed 1 mm below the orifice. This combination warrants direct testing of exchange, cleaning, pressure, extrusion, and temperature; the present velocity data alone do not justify a clinical parameter recommendation.

References

1. Zehnder M (2006) Root canal irrigants. J Endod 32:389–398. https://doi.org/10.1016/j.joen.2005.09.014
2. Haapasalo M, Shen Y, Qian W, Gao Y (2010) Irrigation in endodontics. Dent Clin North Am 54:291–312. https://doi.org/10.1016/j.cden.2009.12.001
3. Boutsioukis C, Arias-Moliz MT (2022) Present status and future directions – irrigants and irrigation methods. Int Endod J 55(Suppl 3):588–612. https://doi.org/10.1111/iej.13739
4. Boutsioukis C, Arias-Moliz MT, Chávez de Paz LE (2022) A critical analysis of research methods and experimental models to study irrigants and irrigation systems. Int Endod J 55(Suppl 2):295–329. https://doi.org/10.1111/iej.13710
5. van der Sluis LWM, Versluis M, Wu MK, Wesselink PR (2007) Passive ultrasonic irrigation of the root canal: a review of the literature. Int Endod J 40:415–426. https://doi.org/10.1111/j.1365-2591.2007.01243.x
6. De Groot SD, Verhaagen B, Versluis M, Wu MK, Wesselink PR, van der Sluis LWM (2009) Laser-activated irrigation within root canals: cleaning efficacy and flow visualization. Int Endod J 42:1077–1083. https://doi.org/10.1111/j.1365-2591.2009.01634.x
7. Blanken J, De Moor RJG, Meire M, Verdaasdonk R (2009) Laser induced explosive vapor and cavitation resulting in effective irrigation of the root canal. Part 1: A visualization study. Lasers Surg Med 41:514–519. https://doi.org/10.1002/lsm.20798
8. Matsumoto H, Yoshimine Y, Akamine A (2011) Visualization of irrigant flow and cavitation induced by Er:YAG laser within a root canal model. J Endod 37:839–843. https://doi.org/10.1016/j.joen.2011.02.035
9. Lukač N, Zadravec J, Gregorčič P, Lukač M, Jezeršek M (2016) Wavelength dependence of photon-induced photoacoustic streaming technique for root canal irrigation. J Biomed Opt 21:075007. https://doi.org/10.1117/1.JBO.21.7.075007
10. Lukač M, Lukač N, Jezeršek M (2020) Characteristics of bubble oscillations during laser-activated irrigation of root canals and method of improvement. Lasers Surg Med 52:907–915. https://doi.org/10.1002/lsm.23226
11. Lukač N, Gregorčič P, Jezeršek M (2016) Optodynamic phenomena during laser-

activated irrigation within root canals. Int J Thermophys 37:66. https://doi.org/10.1007/s10765-016-2071-z
12. Swimberghe RCD, Tzourmanas R, De Moor RJG, Braeckmans K, Coenye T, Meire MA (2022) Explaining the working mechanism of laser-activated irrigation and its action on microbial biofilms: a high-speed imaging study. Int Endod J 55:1372–1384. https://doi.org/10.1111/iej.13824
13. Meire M, De Moor RJG (2024) Principle and antimicrobial efficacy of laser-activated irrigation: a narrative review. Int Endod J 57:841–860. https://doi.org/10.1111/iej.14042
14. Meire M, van Aelst B, Sehovic A, Deari S, Zehnder M (2024) Solutes in water affect the primary cavitation bubble generated by a pulsed erbium-doped yttrium aluminium garnet laser. Lasers Med Sci 39:298. https://doi.org/10.1007/s10103-024-04257-y
15. Koch JD, Jaramillo DE, DiVito E, Peters OA (2016) Irrigant flow during photon-induced photoacoustic streaming (PIPS) using particle image velocimetry (PIV). Clin Oral Investig 20:381–386. https://doi.org/10.1007/s00784-015-1562-9
16. Aung NPS, Watanabe S, Kouno A, Hongo T, Yao K, Satake K, Okiji T (2020) Fluid movement in the apical area beyond the ledge during Er:YAG laser-activated irrigation: a particle image velocimetry analysis. Photobiomodul Photomed Laser Surg 38:438–443. https://doi.org/10.1089/photob.2019.4758
17. Su Z, Li Z, Shen Y, Bai Y, Zheng Y, Pan C, Hou B (2021) Characteristics of the irrigant flow in a simulated lateral canal under two typical laser-activated irrigation regimens. Lasers Surg Med 53:587–594. https://doi.org/10.1002/lsm.23317
18. Li Z, Su Z, Liu H, Bai Y, Shen Y, Pan C (2024) Phase-locked μPIV analysis of flow dynamics in a simulated root canal with different laser-activated irrigations. Lasers Med Sci 39:112. https://doi.org/10.1007/s10103-024-04051-w
19. Jezeršek M, Lukač N, Lukač M (2021) Measurement of simulated debris removal rates in an artificial root canal to optimize laser-activated irrigation parameters. Lasers Surg Med 53:411–417. https://doi.org/10.1002/lsm.23297
20. De Moor RJG, Meire M, Goharkhay K, Moritz A, Vanobbergen J (2010) Efficacy of ultrasonic versus laser-activated irrigation to remove artificially placed dentin debris plugs. J Endod 36:1580–1583. https://doi.org/10.1016/j.joen.2010.06.007
21. Boutsioukis C, Verhaagen B, Versluis M, Kastrinakis E, van der Sluis LWM (2010) Irrigant flow in the root canal: experimental validation of an unsteady computational fluid dynamics model using high-speed imaging. Int Endod J 43:393–403. https://doi.org/10.1111/j.1365-2591.2010.01692.x
22. Boutsioukis C, Lambrianidis T, Kastrinakis E (2009) Irrigant flow within a prepared root canal using various flow rates: a computational fluid dynamics study. Int Endod J 42:144–155. https://doi.org/10.1111/j.1365-2591.2008.01503.x
23. Boutsioukis C, Verhaagen B, Versluis M, Kastrinakis E, Wesselink PR, van der Sluis LWM (2010) Evaluation of irrigant flow in the root canal using different needle types by an unsteady computational fluid dynamics model. J Endod 36:875–879. https://doi.org/10.1016/j.joen.2009.12.026
24. Rito Pereira M, Silva G, Semião V, Silvério V, Martins JNR, Pascoal-Faria P, Alves N, Dias JR, Ginjeira A (2022) Experimental validation of a computational fluid

dynamics model using micro-particle image velocimetry of the irrigation flow in confluent canals. Int Endod J 55:1394–1403. https://doi.org/10.1111/iej.13827
25. Boutsioukis C, Verhaagen B, van der Sluis LWM, Versluis M (2022) Irrigant flow in the root canal during ultrasonic activation: a numerical fluid-structure interaction model and its validation. Int Endod J 55:938–949. https://doi.org/10.1111/iej.13791
26. Koulogiannis A, Walmsley AD, Angeli P, Balabani S (2024) Ultrasonic irrigation flows in root canals: effects of ultrasound power and file insertion depth. Sci Rep 14:5368. https://doi.org/10.1038/s41598-024-54611-x
27. Koch JD, Smith NA, Garces D, Gao L, Olsen FK (2014) In vitro particle image velocity measurements in a model root canal: flow around a polymer rotary finishing file. J Endod 40:412–416. https://doi.org/10.1016/j.joen.2013.10.038
28. Layton G, Wu WI, Selvaganapathy PR, Friedman S, Kishen A (2015) Fluid dynamics and biofilm removal generated by syringe-delivered and two ultrasonic-assisted irrigation methods: a novel experimental approach. J Endod 41:884–889. https://doi.org/10.1016/j.joen.2015.01.027
29. Sarp ASK, Gulsoy M (2017) Determining the optimal dose of 1940-nm thulium fiber laser for assisting the endodontic treatment. Lasers Med Sci 32:1507–1516. https://doi.org/10.1007/s10103-017-2272-0
30. Hale GM, Querry MR (1973) Optical constants of water in the 200-nm to 200-µm wavelength region. Appl Opt 12:555–563. https://doi.org/10.1364/AO.12.000555
31. He X, Li Y, Nie M, Yu Y, Chen H, Pan C, Zhao J (2023) Transient apical peak pressure measurement of Er:YAG laser-activated irrigation in different in vitro tooth models using a high-frequency sensor system. Lasers Med Sci 38:123. https://doi.org/10.1007/s10103-023-03779-1
32. Jezeršek M, Lukač N, Lukač M, Tenyi A, Olivi G, Fidler A (2020) Measurement of pressures generated in root canal during Er:YAG laser-activated irrigation. Photobiomodul Photomed Laser Surg 38:625–631. https://doi.org/10.1089/photob.2019.4776
33. Adrian RJ (1991) Particle-imaging techniques for experimental fluid mechanics. Annu Rev Fluid Mech 23:261–304. https://doi.org/10.1146/annurev.fl.23.010191.001401
34. Keane RD, Adrian RJ (1992) Theory of cross-correlation analysis of PIV images. Appl Sci Res 49:191–215. https://doi.org/10.1007/BF00384623
35. Westerweel J, Scarano F (2005) Universal outlier detection for PIV data. Exp Fluids 39:1096–1100. https://doi.org/10.1007/s00348-005-0016-6
36. Sciacchitano A, Wieneke B, Scarano F (2013) PIV uncertainty quantification by image matching. Meas Sci Technol 24:045302. https://doi.org/10.1088/0957-0233/24/4/045302
37. Nobach H, Bodenschatz E (2009) Limitations of accuracy in PIV due to individual variations of particle image intensities. Exp Fluids 47:27–38. https://doi.org/10.1007/s00348-009-0627-4
38. Hurlbert SH (1984) Pseudoreplication and the design of ecological field experiments. Ecol Monogr 54:187–211. https://doi.org/10.2307/1942661
39. Lazic SE (2010) The problem of pseudoreplication in neuroscientific studies: is it

affecting your analysis? BMC Neurosci 11:5. https://doi.org/10.1186/1471-2202-11-5
40. Aarts E, Verhage M, Veenvliet JV, Dolan CV, van der Sluis S (2014) A solution to dependency: using multilevel analysis to accommodate nested data. Nat Neurosci 17:491–496. https://doi.org/10.1038/nn.3648
41. Hunter JD (2007) Matplotlib: A 2D graphics environment. Comput Sci Eng 9:90–95. https://doi.org/10.1109/MCSE.2007.55
42. Thielicke W, Stamhuis EJ (2014) PIVlab – towards user-friendly, affordable and accurate digital particle image velocimetry in MATLAB. J Open Res Softw 2:e30. https://doi.org/10.5334/jors.bl